Neurobiology of Disease

Motor Impairments and Dopaminergic Defects Caused by Loss of Leucine-Rich Repeat Kinase Function in Mice

Guodong Huang,[1] Daniel W. Bloodgood,[3] Jongkyun Kang,[1] Anu Shahapal,[1] Phoenix Chen,[1] Konstantin Kaganovsky,[3] Jae-Ick Kim,[3] Jun B. Ding,[3,4] and Jie Shen[1,2]

[1]Department of Neurology, Brigham and Women's Hospital, Harvard Medical School, Boston, Massachusetts 02115, [2]Program in Neuroscience, Harvard Medical School, Boston, Massachusetts 02115, [3]Departments of Neurosurgery and, and [4]Neurology and Neurological Sciences, Stanford University School of Medicine, Stanford, California 94305

Mutations in leucine-rich repeat kinase 2 (LRRK2) are the most common genetic cause of Parkinson's disease (PD), but the pathogenic mechanism underlying LRRK2 mutations remains unresolved. In this study, we investigate the consequence of inactivation of LRRK2 and its functional homolog LRRK1 in male and female mice up to 25 months of age using behavioral, neurochemical, neuropathological, and ultrastructural analyses. We report that *LRRK1* and *LRRK2* double knock-out (*LRRK* DKO) mice exhibit impaired motor coordination at 12 months of age before the onset of dopaminergic neuron loss in the substantia nigra (SNpc). Moreover, *LRRK* DKO mice develop age-dependent, progressive loss of dopaminergic terminals in the striatum. Evoked dopamine (DA) release measured by fast-scan cyclic voltammetry in the dorsal striatum is also reduced in the absence of LRRK. Furthermore, *LRRK* DKO mice at 20–25 months of age show substantial loss of dopaminergic neurons in the SNpc. The surviving SNpc neurons in *LRRK* DKO mice at 25 months of age accumulate large numbers of autophagic and autolysosomal vacuoles and are accompanied with microgliosis. Surprisingly, the cerebral cortex is unaffected, as shown by normal cortical volume and neuron number as well as unchanged number of apoptotic cells and microglia in *LRRK* DKO mice at 25 months. These findings show that loss of LRRK function causes impairments in motor coordination, degeneration of dopaminergic terminals, reduction of evoked DA release, and selective loss of dopaminergic neurons in the SNpc, indicating that *LRRK* DKO mice are unique models for better understanding dopaminergic neurodegeneration in PD.

Key words: **dopamine release; knock-out mice; LRRK2; Parkinson's disease; SNpc; striatum**

Significance Statement

Our current study employs a genetic approach to uncover the normal function of the LRRK family in the brain during mouse life span. Our multidisciplinary analysis demonstrates a critical normal physiological role of LRRK in maintaining the integrity and function of dopaminergic terminals and neurons in the aging brain, and show that *LRRK* DKO mice recapitulate several key features of PD and provide unique mouse models for elucidating molecular mechanisms underlying dopaminergic neurodegeneration in PD.

Introduction

Parkinson's disease (PD) is the most common neurodegenerative movement disorder characterized clinically by resting tremor, rigidity, bradykinesia, and postural instability. The neuropathological features of PD include the loss of dopaminergic neurons and the presence of α-synuclein-rich Lewy bodies in the substantia nigra pars compacta (SNpc) as well as degeneration of dopaminergic terminals in the striatum. Mutations in the *leucine-rich repeat kinase 2* (*LRRK2*) gene are the most common cause of both familial and sporadic PD, highlighting its importance in PD pathogenesis (Paisán-Ruíz et al., 2004; Shen, 2004; Zimprich et al., 2004; Di Fonzo et al., 2005; Gilks et al., 2005; Hernandez et al., 2005; Kachergus et al., 2005; Nichols et al., 2005; Zabetian et al., 2005; Mata et al., 2005a, b; Lesage et al., 2007; Hatano et al., 2014; Takanashi et al., 2018; Kluss et al., 2019; Shu et al., 2019). However, the pathogenic mechanism underlying LRRK2 mutations remains unresolved.

LRRK2 is an evolutionarily conserved large protein containing multiple functional domains, including a Ras-of-complex

Received Jan. 19, 2022; revised Mar. 31, 2022; accepted Apr. 20, 2022.

Author contributions: J.B.D. and J.S. designed research; G.H., D.W.B., J.K., A.S., P.C., K.K., and J.-I.K. performed research; G.H., D.W.B., and J.K. analyzed data; and G.H., J.K., J.B.D., and J.S. wrote the paper.

This work was supported by grants from the National Institutes of Health (R01NS071251 and P50NS091857 to J.S.). We thank Sanghun Lee for advice on statistical analysis, Huailong Zhao for technical assistance, and the Shen lab members for discussion.

J.S. has financial interests in iNeuro Therapeutics and Paros Biosciences, which develop therapies for Alzheimer's disease; J.K. consults for iNeuro Therapeutics; and the interests of J.S. and J.K. are managed by Mass General Brigham in accordance with the institutional conflict of interest policies. All the other authors declare no competing financial interests.

Correspondence should be addressed to Jie Shen at jshen@bwh.harvard.edu.

https://doi.org/10.1523/JNEUROSCI.0140-22.2022

(ROC) GTPase domain and a kinase domain, where all pathogenic mutations reside (Bosgraaf and Van Haastert, 2003; Roosen and Cookson, 2016). The R1441 residue in the ROC domain harbors at least three independent PD mutations (R1441C/G/H), suggesting that this Arg residue is particularly important for LRRK2 function and PD pathogenesis (Zimprich et al., 2004; Zabetian et al., 2005; Mata et al., 2005a, b; Hatano et al., 2014; Takanashi et al., 2018). G2019S in the kinase domain is the most common mutation, representing up to 10% in familial PD cases and ~1% in idiopathic cases (Di Fonzo et al., 2005; Gilks et al., 2005; Hernandez et al., 2005; Kachergus et al., 2005; Nichols et al., 2005). LRRK2 has been implicated in vesicular trafficking, possibly mediated through phosphorylation of a subset of Rab GTPases, regulators of membrane trafficking (Cookson, 2016; Vidyadhara et al., 2019; Erb and Moore, 2020).

Our previous genetic studies revealed that LRRK2 regulates the autophagy-lysosomal pathway and homeostasis of α-synuclein (Tong et al., 2010; 2012). *LRRK2*$^{-/-}$ mice develop PD-like phenotypes prominently in the aged kidney, including autophagy impairment, accumulation of α-synuclein, and increases of apoptosis and inflammatory responses. The lack of brain phenotypes in *LRRK2*$^{-/-}$ mice may be because of the presence of LRRK1, a functional homolog of LRRK2 that is broadly expressed in the brain including the midbrain (https://www.proteinatlas.org/ENSG00000154237-LRRK1/brain). Indeed, inactivation of both LRRK1 and LRRK2 in *LRRK* double knock-out (DKO) mice results in age-dependent, progressive loss of dopaminergic neurons in the SNpc, beginning at 14 months of age (Giaime et al., 2017).

In the current study, we performed behavioral analysis and fast-scan cyclic voltammetry (FSCV) as well as quantitative neuropathological and ultrastructural assessment of *LRRK* DKO female and male mice up to 25 months of age. We found that *LRRK* DKO mice display impaired motor coordination, as indicated by increases of hindlimb slips and traversal time in the beam walk test. histological analysis also showed age-dependent loss of dopaminergic terminals in the striatum of *LRRK* DKO mice. Furthermore, fast-scan cyclic voltammetry analysis revealed an age-dependent reduction in evoked dopamine (DA) release in the dorsal striatum of *LRRK* DKO mice. By 20–25 months of age, *LRRK* DKO mice show substantial loss of dopaminergic neurons in the SNpc and increases of apoptosis. The surviving neurons in the SNpc accumulate large numbers of electron-dense autophagic vacuoles and are accompanied with increases of microgliosis. However, the cerebral cortex of *LRRK* DKO mice is still unaffected at 25 months of age, as evidenced by normal cortical volume and neuron number as well as unchanged number of apoptotic cells and microglia. These results together demonstrate the importance of LRRK in dopaminergic neuron function and survival.

Materials and Methods

Mice. The generation and characterization of *LRRK1*$^{-/-}$, *LRRK2*$^{-/-}$, and *LRRK* DKO mice have been described previously (Tong et al., 2010; Giaime et al., 2017). We regularly bred *LRRK* DKO (*LRRK1*$^{-/-}$; *LRRK2*$^{-/-}$) mice with C57BL/6J and 129 F1 hybrid (B6/129 F1) wild-type mice to obtain *LRRK1*$^{+/-}$; *LRRK2*$^{+/-}$ mice, which were then interbred to obtain *LRRK1*$^{-/-}$; *LRRK2*$^{-/-}$ mice. All mice were housed in humidity- and temperature-controlled rooms under 12/12 h light/dark cycle with standard rodent chow and water. All procedures were approved by the Institutional Animal Care and Use Committees of Brigham and Women's Hospital and Stanford University, in accordance with the U.S. Department of Agriculture Animal Welfare Act, Public Health Service *Policy on Humane Care and Use of Laboratory Animals*, the Institute for Laboratory Animal Research *Guide for the Care and Use of Laboratory Animals*, and other applicable laws and regulations. Both male and female mice were used in each experiment. All experiments were performed in a genotype blind manner.

PCR genotyping. Tail genomic DNA was extracted at postnatal days 10–12. The primers used to differentiate the wild-type (WT) or deleted *LRRK1* allele are mK1F13 (5′- GGCTACTGAACTGGATGCTGGC, forward primer in *LRRK1* exon 5), mK1U1 (5′- CACTGCATTCTAGTTGT GGTTTGTCC, forward primer in the *SV40* poly A of the *En2SA-IRES-lacZ* cassette inserted into *LRRK1* intron 3, which is located 5′ to the most upstream *loxP* site in intron 3), and mK1R9 (5′- GCATGATG GAATCCGATTGTAATCTC, reverse primer in *LRRK1* intron 5 located downstream of the *loxP* site in intron 5). The 509 bp PCR product amplified using mK1F13 (exon 5) and mK1R9 (intron 5) represents the wild-type *LRRK1* allele. The 241 bp fragment amplified using mK1U1 (*SV40* poly A) and mK1R9 (*LRRK1* intron 5) represents the deleted *LRRK1* allele, resulting from Cre-mediated site-specific recombination between the two external *loxP* sites to remove the *PGK-Neo* cassette and *LRRK1* exons 4–5.

The primers used to differentiate the wild-type or deleted *LRRK2* allele are mF80 (5′- GGCTCTGAAGAAGTTGATAGTCAGGCTG, forward primer in *LRRK2* exon 1), mF82 (5′- GAACTTCTGTCTGC AGCCATCATC, forward primer in the *LRRK2* promoter), and mR52 (5′- CTGTACACTGGCAACTCTCATGTAGGAG, reverse primer in *LRRK2* exon 2). The 375 bp PCR product amplified using primers mF80 (exon 1) and mR52 (exon 2) represents the wild-type *LRRK2* allele, whereas the 580 bp PCR product amplified using primers mF82 (promoter) and mR52 (exon 2) represents the deleted *LRRK2* allele.

Behavior analysis. LRRK DKO mice and wild-type controls at 12 and 24 months of age were used. Mice were acclimated in the behavioral facility for a minimum of 7 d and were then individually handled daily for 5 d before testing. Mice were coded so the experimenter was unaware of their genotypes until the data analysis was complete. After the completion of behavioral experiments, mice were used for histological analysis.

Beam walk test. A Plexiglas beam 100 cm in length (Plastic Zone), 20 mm or 10 mm in width, was raised 60 cm above a table, and safety bedding was placed under the beam to avoid any harm in case of falls. Mice were placed onto the starting point of the beam in bright light, and the time (in seconds) to reach their home cage on the other darker side of the beam (~80 cm in distance) as well as the hindpaw slips (number of hindlimb errors) were recorded. Mice were trained three trials per day for 2 consecutive days to traverse the 20 mm beam (without the wire mesh) to their home cage. On the test day, mice were trained further with two additional trials on the 20 mm beam (without the wire mesh). Mice were then tested in two successive trials on the 20 mm beam (with the wire mesh) followed by two consecutive test trials on the 10 mm beam (with the wire mesh). All test trials were videotaped, and the travel time and the number of hindlimb errors were recorded. Mice fell off the beam during both trials or stalled on the beam for >120 s during the test were excluded. Between trials mice were placed in the home cage for 2 min to rest.

Pole test. The pole test was performed following previous reports (Matsuura et al., 1997; Goldberg et al., 2003) with minor modifications. Mice were placed on top of the pole (60 cm in height, 10 mm in diameter) with their head facing upward, and the base of the pole was placed in the home cage. Mice were trained three trials per day for 2 d to traverse the pole to the cage floor and were further trained two trials before testing on the test day. Mice were then tested for 2 trials, and the time to turn around (turning time) and the time to descend the pole (descending time) were recorded. Mice that stalled on the top of the pole for >120 s were excluded. Between trials, mice were placed in the home cage for 2 min to rest.

Rotarod test. The procedures of the rotarod have been described previously (Goldberg et al., 2003). Briefly, four mice at a time were placed on an Economex accelerating rotarod (Columbus Instruments) equipped with individual timers for each mouse. Mice were initially trained to stay on the rod at a constant rotation speed of 5 rpm. After a 2 min rest, mice that had fallen were repeatedly placed back on the rotarod until they were able to stay on the rotating rod for at least 2 min.

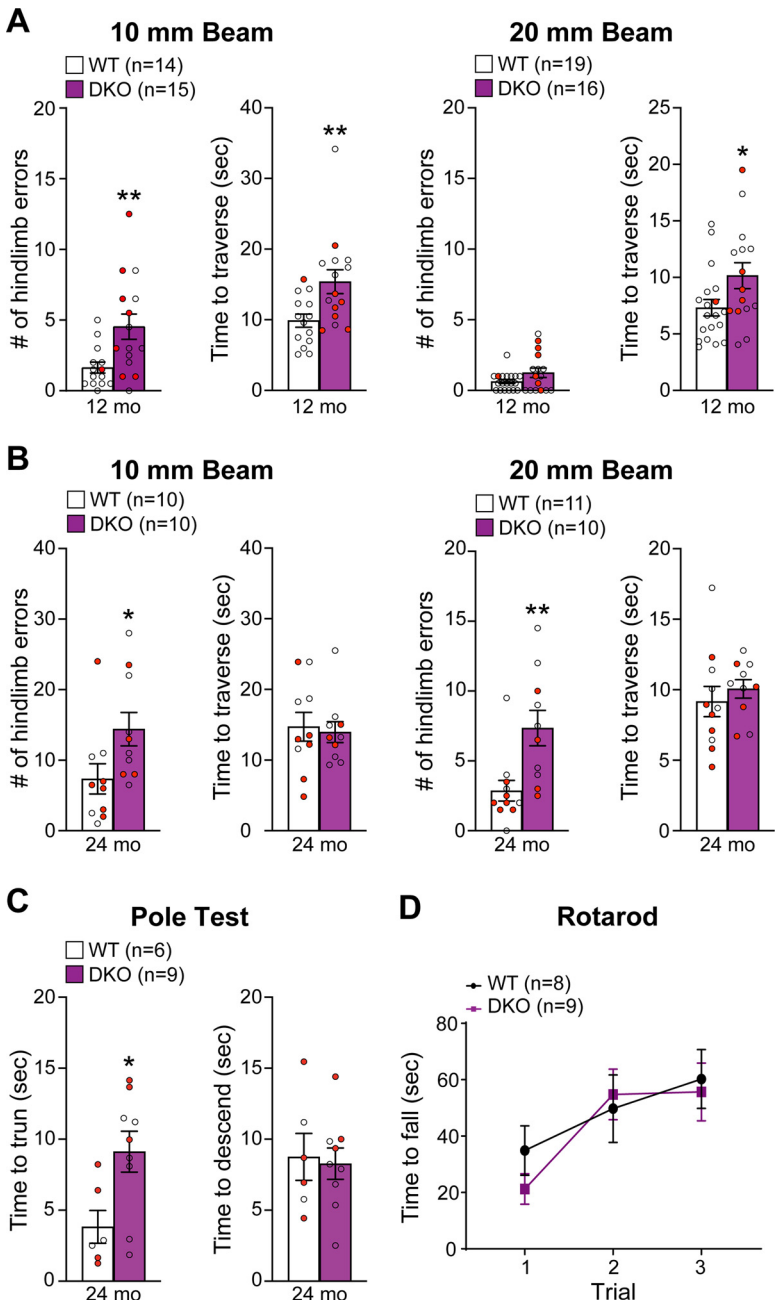

Figure 1. Impairment of motor coordination in *LRRK* DKO mice. ***A***, In the 10 mm beam walk test, compared to WT mice, *LRRK* DKO mice at 12 months of age show significantly more hindlimb slips (WT, 1.6 ± 0.4; DKO, 4.5 ± 0.9; $p = 0.0074$, unpaired two-tailed Student's *t* test) and longer traversal time (WT, 9.9 ± 0.9 s; DKO, 15.4 ± 1.7 s; $p = 0.0093$). In the less challenging 20 mm beam walk test, *LRRK* DKO mice display few hindlimb slips (WT, 0.6 ± 0.1; DKO, 1.3 ± 0.3; $p = 0.0835$) but longer traversal time (WT, 7.3 ± 0.7 s; DKO, 10.3 ± 1.1 s; $p = 0.0268$). ***B***, At 24 months of age, relative to WT mice, *LRRK* DKO mice exhibit markedly more hindlimb errors while traversing the 10 mm beam (WT, 7.4 ± 2.1; DKO, 14.4 ± 2.4; $p = 0.0404$; unpaired two-tailed Student's *t* test), but there is no difference in the time to traverse the beam (WT, 14.7 ± 2.0 s; DKO, 14.0 ± 1.5; $p = 0.7678$). In the 20 mm beam walk test, *LRRK* DKO mice (7.4 ± 1.3) show more hindlimb slips compared with WT controls (2.9 ± 0.7, $p = 0.0056$), but there is no difference in traversal time (WT, 9.2 ± 1.1 s; DKO, 10.1 ± 0.7 s; $p = 0.4929$). ***A***, ***B***, Within the WT or DKO group, there is no significant difference between male and female mice in their performance ($p > 0.05$). Mice that stalled >120 s on the beam or fell off the beam during both trials were excluded. ***C***, In the pole test, *LRRK* DKO mice (9.1 ± 1.4 s) at 24 months of age exhibit significantly longer turning time than WT mice (3.8 ± 1.2 s, $p = 0.0204$, unpaired two-tailed Student's *t* test), but there is no sex-specific difference within the genotypic group ($p > 0.05$; specific *p* values can be found in in Extended Data Figure 1-1). The descending time is similar between WT (8.8 ± 1.7 s) and DKO (8.3 ± 1.1 s, $p = 0.8053$) mice, but the descending time of male DKO mice is significantly longer than that of female DKO mice ($p = 0.0466$). ***D***, In the rotarod test, *LRRK* DKO (Trial 1, 21.2 ± 5.4 s; Trial 2, 54.8 ± 9.0 s; Trial 3, 55.7 ± 10.2 s) and WT mice (Trial 1, 34.9 ± 8.8 s; Trial 2, 49.8 ± 12.0 s; Trial 3, 60.3 ± 10.4 s) show similar latencies to fall off an accelerating rotating rod ($F_{(1,15)} = 0.1351$, $p = 0.7183$; Trial 1, $p = 0.9334$; Trial 2, $p > 0.9999$; Trial 3, $p > 0.9999$, two-way ANOVA with Bonferroni's *post hoc* multiple comparisons). The average time before falling off the rod is shown for each of the three consecutive trials. All data are expressed as mean ± SEM. Red filled and open circles represent data obtained from individual male and female mice, respectively; $^*p < 0.05$, $^{**}p < 0.01$.

Following training, mice were subsequently tested by placing them on the rod at a rotation speed of 5 rpm, and as the rod accelerated by 0.2 rpm/s, the latency to fall was measured. Mice were tested for a total of three trials. Between trials, mice were placed in the home cage for 2 min to rest.

Fast-scan cyclic voltammetry. Coronal brain sections (300 μm) were used for FSCV experiments. Mice were anesthetized with isoflurane and decapitated, and the brain was then quickly removed and exposed to chilled artificial CSF (ACSF) containing the following (in mM): 125 NaCl, 2.5 KCl, 1.25 NaH_2PO_4, 25 $NaHCO_3$, 15 glucose, 2 $CaCl_2$ and 1 $MgCl_2$ oxygenated with 95% O_2 and 5% CO_2 (300-305 mOsm, pH 7.4). A tissue vibratome (Leica VT1200) was used to section the chilled brain, producing brain slices containing dorsal striatum. Acute brain slices were first kept in ACSF for 30 min at 34°C and then maintained for another 30 min at room temperature. After a recovery period, slices were moved to a submerged recording chamber perfused with ACSF at a rate of 2-3 ml/min at 30-31°C, and brain slices were recorded within 4 h after recovery.

Extracellular DA release was monitored by fast-scan cyclic voltammetry recordings performed in the dorsal striatum using carbon-fiber microelectrodes (7 μm diameter carbon fiber extending 50-100 μm beyond the tapered glass seal). Cyclic voltammograms were measured with a triangular potential waveform (−0.4 to +1.3 V vs Ag/AgCl reference electrode, 400 V/s scan rate, 8.5 ms waveform width) applied at 100 ms intervals. The carbon fiber microelectrode was held at −0.4 V between scans. Cyclic voltammograms were background subtracted by averaging 10 background scans. Each striatal hemisphere was recorded in both dorsal lateral and dorsal medial striatum, and the order of recording was counterbalanced across slices. Dopaminergic axon terminals were stimulated locally (100–200 μm from carbon fiber) using concentric electrodes (Frederick Haer) at 100 μA. First, each recording site received two electrical stimulations separated by 15 s; after 2 min of recovery time, the same site received a train of stimulation (five pulses at 25 Hz). Evoked DA release and subsequent oxidation current were detected and monitored using a custom built potentiostat (University of Washington, Seattle) and TarHeel CV written in LabVIEW (National Instruments). Evoked DA concentration by electrical stimulation was quantified by plotting the peak oxidation current of the voltammogram over time. The carbon fiber electrode was calibrated at the end of each day of experiments to convert oxidation current to dopamine concentration using 10 μM DA in ACSF.

Histological analysis. Mice were anesthetized with ketamine (100 mg/kg) plus xylazine

←

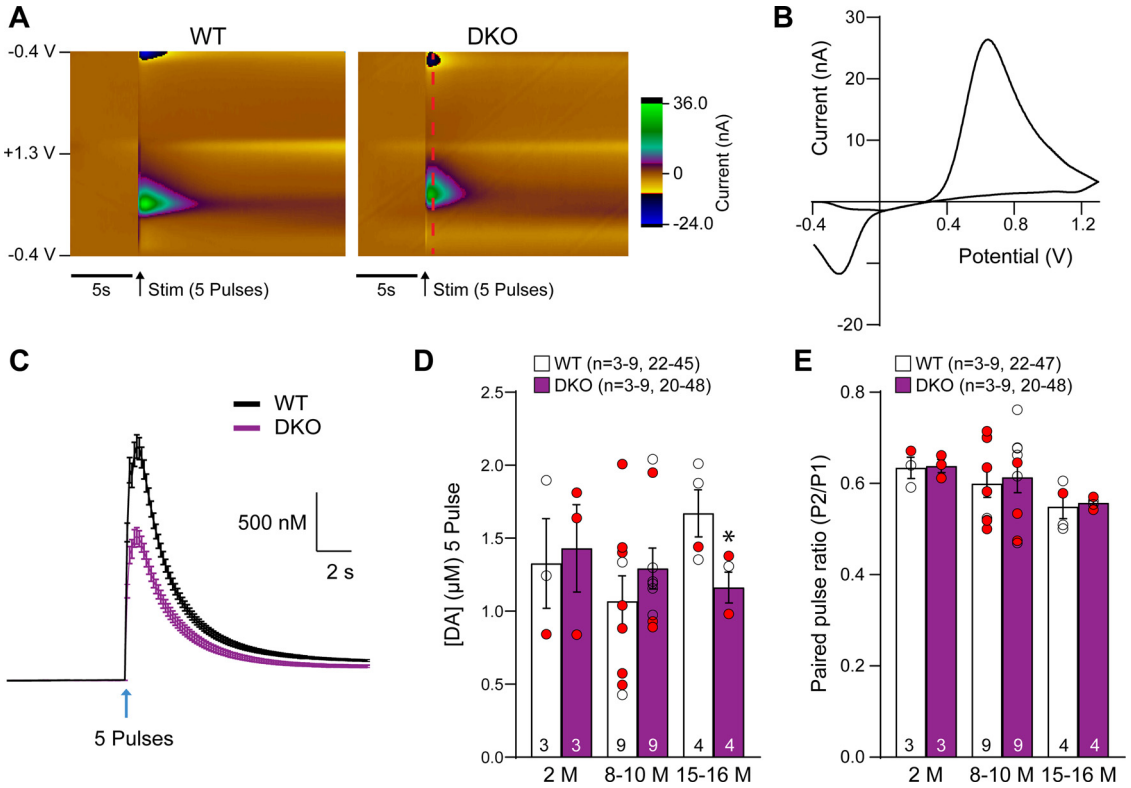

Figure 2. Age-dependent impairment of evoked DA release in the striatum of *LRRK* DKO mice. ***A***, Representative 3D voltammograms from five-pulse stimulation in striatal slices of WT and *LRRK* DKO mice at 15–16 months of age; *x*-axis, recording time; *y*-axis, applied potential; color map, recorded current. Arrows represent time of stimulation. ***B***, Two-dimensional current versus voltage plot showing oxidation and reduction peaks of DA (cross section at the dashed line in ***A***). ***C***, Summary of FSCV recordings measured at the peak oxidative voltage evoked by five-pulses stimulations in slices from *LRRK* DKO and WT mice at 15–16 months of age. ***D***, Quantification of peak DA release electrically evoked by 5 pulses (25 Hz) in the dorsal striatum in *LRRK* DKO and WT mice at 2 months of age (WT, 1.33 ± 0.31 μM; DKO, 1.43 ± 0.30 μM; $p = 0.8225$, unpaired two-tailed Student's *t* test), 8–10 months (WT, 1.07 ± 0.18 μM; DKO, 1.29 ± 0.14 μM; $p = 0.3314$), and 15–16 months (WT, 1.67 ± 0.16 μM; DKO, 1.16 ± 0.11 μM; $p = 0.0385$) show a significant reduction of DA concentration in striatal slices from *LRRK* DKO mice at 15–16 months. ***E***, Quantification of paired-pulse ratios (PPR) determined by FSCV shows normal PPR at the ages of 2 months ($p = 0.8898$, unpaired two-tailed Student's *t* test), 8–10 months ($p = 0.7619$), and 15–16 months ($p = 0.7560$). The paired-pulse ratio values were calculated by measuring the peak oxidative voltage evoked by each pulse and computing the ratio of the second pulse divided by the first pulse. The value in the column indicates the number of the mice used in each experiment. The number in the parentheses indicates the number of mice and the number of evoked recordings. All data are expressed as mean ± SEM. Red filled and open circles represent data obtained from individual male and female mice, respectively, and there is no sex-specific difference within the genotypic group ($p > 0.05$; specific *p* values can be found in Extended Data Figure 2-1); *$p < 0.05$.

(10 mg/kg) plus acepromazine (3 mg/kg), and transcardially perfused with PBS, pH 7.4, containing 0.25 × g/L heparin (Sigma-Aldrich) and 5 × g/L procaine (Sigma-Aldrich). Brains were dissected out and postfixed in 4% formaldehyde in PBS (Electron Microscopy Sciences) at 4°C overnight and then processed for paraffin embedding following standard procedures. Serial sagittal sections (10 μm) and coronal sections (16 μm) were obtained using a Leica RM2235 microtome. Immunohistochemical analysis was performed as previously described (Schindelin et al., 2012; Yamaguchi and Shen, 2013; Kang et al., 2021). The primary antibodies used were rabbit anti-tyrosine hydroxylase (TH; 1:750; catalog #ab112, Abcam; RRID:AB_297840), mouse anti-NeuN (1:400; catalog# MAB377, Millipore; RRID:AB_2298772), rabbit anti-cleaved caspases-3 (1:150; catalog #9661, Cell Signaling Technology; RRID:AB_2341188), rabbit anti-Iba1 (1:500; catalog #019-19751, FUJIFILM Wako Shibayagi; RRID:AB_839504), or mouse anti-TH (1:50; catalog #sc-25269 AF680, Santa Cruz Biotechnology; RRID:AB_628422). The secondary antibodies used were goat biotinylated anti-rabbit IgG (1:250; catalog #BA-1000, Vector Laboratories; RRID:AB_2313606), goat biotinylated anti-mouse IgG (1:250; catalog #BA-9200, Vector Laboratories; RRID:AB_2336171) or Alex Fluor 546 (1:500; catalog #A-11035, Thermo Fisher Scientific; RRID:AB_2534093).

For the quantification of TH immunoreactivity in the striatum, we performed immunostaining using every 10th serial coronal sections (16 μm in thickness) throughout the entire striatum (a total of 12–15 sections, spaced 160 μm apart). The images of TH immunoreactivity in the striatum were captured under 2× objective lens (Olympus BX40, 8-bit RGB camera) using identical parameters (cellSens Entry software) and then analyzed using the Fiji version of ImageJ, and the optical density was determined as previously described (Ruifrok and Johnston, 2001; Schindelin et al., 2012). The mean value of TH immunoreactivity in the striatum of wild-type mice was set as 100%.

Stereology quantification in the SNpc and the cerebral cortex was performed as previously described (Yamaguchi and Shen, 2013; Kang et al., 2021) using the BIOQUANT image analysis software that was connected to the Olympus BX51 microscopy with a charge-coupled device camera. Briefly, for dopaminergic neuron count, TH+ neurons in the SNpc were quantified in every 10th serial coronal sections (16 μm in thickness) throughout the SNpc (a total of 8–10 sections, spaced 160 μm apart) using the fractionator (100 × 100 μm) and optical dissector method (50 μm × 50 μm sampling box), and was then converted as follows: [average number of TH+ neurons in the SNpc counted per section] × 4 (1/4 area sampled: 50 × 50/100 × 100) × [number of sections quantified] × 10 (every 10th sections sampled) × 2 (both hemispheres). The volume of the neocortex per hemisphere was quantified using Nissl-stained serial sections (every 25th coronal sections, spaced 400 μm apart), and the cortical volume was calculated as follows: [the average area of the entire neocortex measured in all sampled sections] × 16 [thickness of the section] × [number of serial sections encompassing the

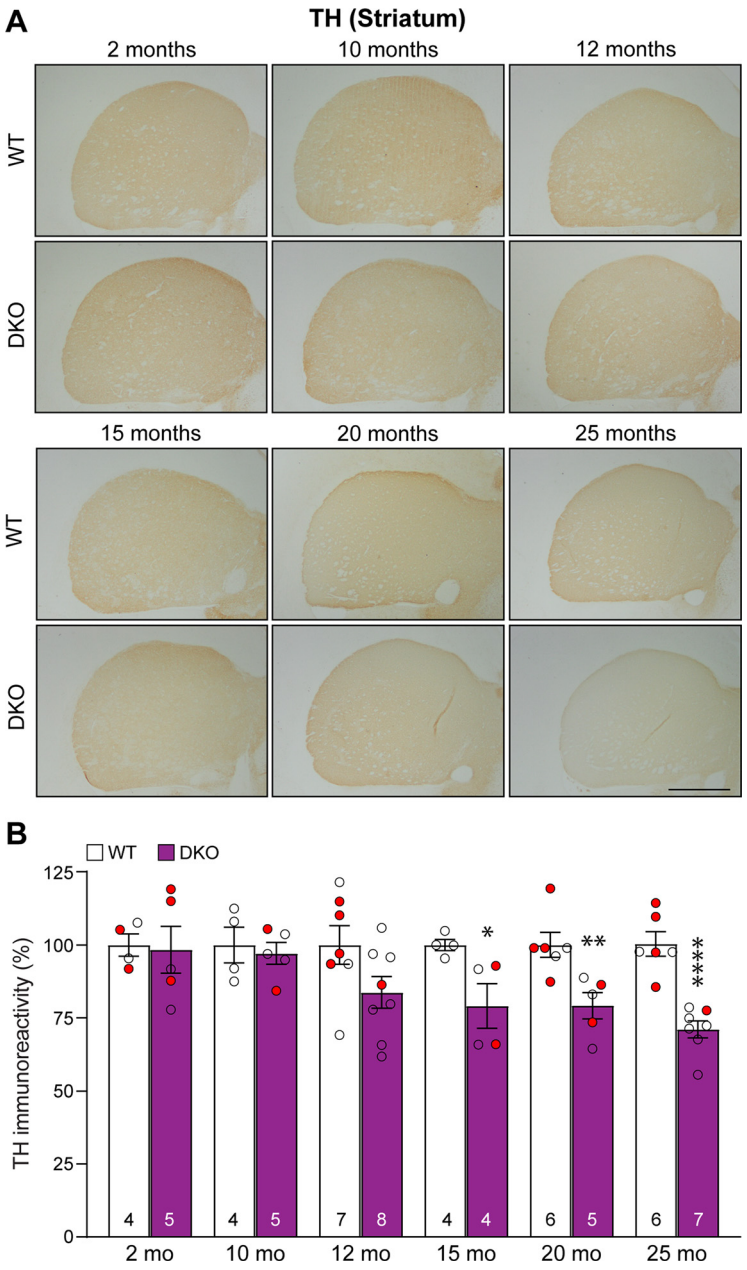

Figure 3. Age-dependent loss of TH+ DA terminals in the striatum of *LRRK* DKO mice. ***A***, Representative TH immunostaining images in the striatum of WT and *LRRK* DKO mice between the ages of 2 and 25 months. ***B***, Quantification of TH immunoreactivity in the striatum of *LRRK* DKO mice and WT controls shows age-dependent decreases of TH immunoreactivity in *LRRK* DKO mice beginning at the age of 12 months (~16%, $p = 0.0781$, unpaired two-tailed Student's *t* test). TH immunoreactivity is further diminished at 15 months (~21%, $p = 0.0378$), 20 months ($p = 0.0088$), and 25 months ($p < 0.0001$). Average TH immunoreactivity in WT controls was defined as 100%. The value in the column indicates the number of the mice used in each experiment. All data are expressed as mean ± SEM. Red filled and open circles represent data obtained from individual male and female mice, respectively, and there is no sex-specific difference within the genotypic group ($p > 0.05$; specific *p* values can be found in Extended Data Figure 3-1); *$p < 0.05$, **$p < 0.01$, ****$p < 0.0001$. Scale bar, 100 μm.

neocortex; ~350 sections per brain]. The number of NeuN+ neurons in the neocortex was quantified in NeuN-stained sections (every 25th coronal sections, spaced 400 µm apart) using the fractionator (500 × 500 µm) and optical dissector (100 µm × 100 µm sampling box). The number of neurons was counted with an indicator of NeuN+ neurons through the 40× objective lens from all sections. The number of neurons in the neocortex per hemisphere was calculated as follows: [total number of NeuN+ neurons counted in all sampled sections] × 25 (1/25 area sampled: 100 × 100/500 × 500) × 25 (every 25th sections sampled).

The number of active Caspase-3+ apoptotic cells was quantified in every 10th serial coronal sections (16 µm in thickness) throughout the SNpc (a total of 8–10 sections, spaced 160 µm apart, six to seven brains per genotype), in every 20th serial sagittal or coronal sections (16 µm in thickness, spaced 320 µm apart) throughout the striatum (a total of sagittal six to eight sections, three brains per genotype) or the neocortex (a total of 19–25 coronal sections, six to eight brains per genotype). Number of active Caspase-3+ cells in the SNpc was calculated by multiplying the total number of active Caspase-3+ cells in the SNpc (one hemisphere) of all sections with 10 (every 10th sections sampled). Number of active Caspase-3+ cells in the striatum or neocortex was calculated by multiplying the total number of active Caspase-3+ cells in the striatum or neocortex (one hemisphere) of all sections with 20 (every 20th sections sampled).

Iba1+ cells in the SNpc were quantified using serial coronal sections (16 µm in thickness, every 10th sections, a total of six to eight sections per brain). The total number of Iba1+ cells in the SNpc, which was marked by TH immunoreactivity, was calculated as follows: [total number of Iba1+ microglia in all six to eight sections] × 10 (every 10th sections sampled) × 2 (both hemispheres). The number of Iba1+ cells in the neocortex was quantified in Iba1-stained sections (every 25th coronal sections, spaced 400 µm apart, a total of 12–15 sections per brain) using the fractionator (500 × 500 µm) and optical dissector (100 µm x 100 µm sampling box). Iba1+ microglia in all sections were counted through a 40× objective lens, and the number of Iba1+ cells in the neocortex was calculated as follows: [total number of Iba1+ microglia in all of the 12–15 sections] × 25 (1/25 area sampled, 100 × 100/500 × 500) × 25 (every 25th sections sampled) × 2 (both hemispheres).

Transmission electron microscopy analysis. The collection and quantification of the electron microscopy (EM) images were performed as described previously (Giaime et al., 2017). Mice were perfused with PBS containing 0.25 × g/L heparin (Sigma-Aldrich) and 5 × g/L procaine (Sigma-Aldrich) followed by a fixative solution including 2.5% paraformaldehyde and 2.5% glutaraldehyde in 0.1 M sodium cacodylate buffer, pH 7.4 (catalog #1549, Electron Microscopy Sciences). After overnight postfixation at 4°C, the dissected tissues were trimmed to 1–2 mm^3 cubes and then embedded and sectioned (~60–80 nm in thickness) at the Harvard Medical School EM facility. EM images were collected on a JEOL 1200EX transmission electron microscope. A minimum of 10 micrographs containing the entire cell body was analyzed for each brain. The number of electron-dense autophagic and lysosomal vacuoles (>0.5 μm in diameter) in individual neuronal profiles was quantified.

Experimental design and statistical analysis. Data acquisition and quantification were performed in a genotype blind manner, and all statistical analyses were performed using Prism 9 (GraphPad) software, ImageJ, or Excel (Microsoft). All data are presented as the means ± SEM. The exact number of mice, neuron profiles, or brains are provided in relevant figures. Statistical analyses were conducted using unpaired

two-tailed Student's *t* test or two-way ANOVA with Bonferroni's *post hoc* multiple comparisons. Statistical outliers were identified and excluded using the ROUT method with 1% the maximum desired false discovery rate developed by Prism (*$p < 0.05$, **$p < 0.01$, ***$p < 0.001$, and ****$p < 0.0001$).

Results

Impairment of motor coordination in *LRRK* DKO mice

To determine whether *LRRK* DKO mice show motor deficits, we performed behavioral analysis of *LRRK* DKO and wild-type mice at 12 months of age using two versions of the elevated beam walk test with varying widths of the beam (Fig. 1*A*). *LRRK* DKO mice displayed significantly more hindlimb slips/errors (4.5 ± 0.9) and longer traversal time (15.4 ± 1.7 s) in the 10 mm beam walk test, relative to wild-type controls, which exhibited fewer slips (1.6 ± 0.4, $p = 0.0074$) and shorter traversal time (9.9 ± 0.9 s, $p = 0.0088$, unpaired two-tailed Student's *t* test; Fig. 1*A*). In the 20 mm beam walk, which is less challenging than the narrower beam walk, both *LRRK* DKO mice (1.3 ± 0.3) and wild-type controls (0.6 ± 0.1, $p = 0.0835$) at 12 months of age performed well with few hindlimb slips, but it took *LRRK* DKO mice (10.3 ± 1.1 s) longer to traverse the beam compared with wild-type mice (7.3 ± 0.7 s, $p = 0.0268$; Fig. 1*A*). These results show that *LRRK* DKO mice at 12 months of age already exhibit deficits in motor coordination.

We then performed the beam walk test in *LRRK* DKO and wild-type mice at 24 months of age (Fig. 1*B*). We found that *LRRK* DKO mice showed significantly higher hindlimb errors in both the 10 mm (WT, 7.4 ± 2.1; DKO, 14.4 ± 2.4; $p = 0.0404$) and the 20 mm (WT, 2.9 ± 0.7; DKO, 7.4 ± 1.3; $p = 0.0056$) versions of the beam walk, but the traverse time is similar between the genotypic groups (Fig. 1*B*). We also tested *LRRK* DKO and wild-type mice at 24 months of age in the pole test, which is sensitive to motor coordination (Goldberg et al., 2003). We found that *LRRK* DKO mice (9.1 ± 1.4 s) showed significantly longer turning time than wild-type mice (3.8 ± 1.2 s, $p = 0.0204$, unpaired two-tailed Student's *t* test), but the descending time to their home cage was similar ($p = 0.8053$; Fig. 1*C*). However, *LRRK* DKO mice performed similarly as wild-type mice in the rotarod test with comparable latencies to fall compared with wild-type controls on the accelerating rotating rod in three independent trials ($F_{(1,15)} = 0.1351$, $p = 0.7183$; Trial 1, $p = 0.9334$; Trial 2, $p > 0.9999$; Trial 3, $p > 0.9999$; two-way ANOVA with

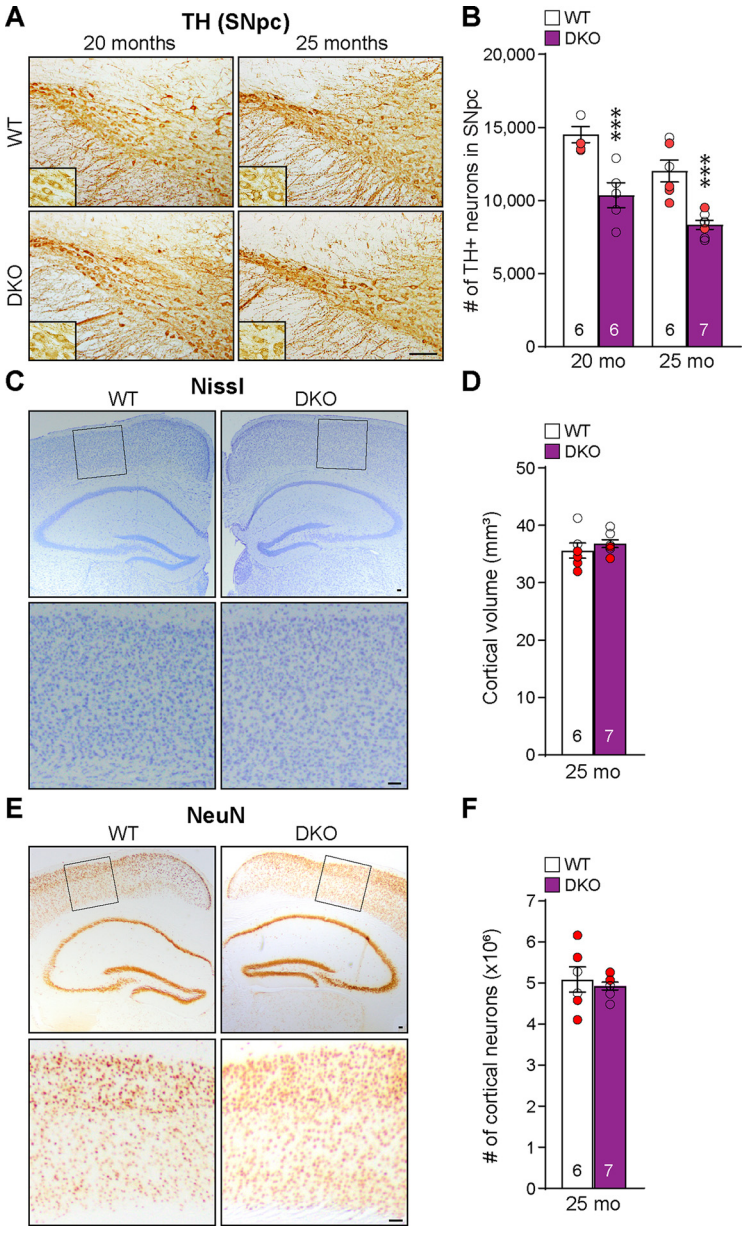

Figure 4. *LRRK* DKO mice at 20–25 months of age develop substantial loss of dopaminergic neurons in the SNpc but exhibit no cortical neurodegeneration. ***A***, Representative coronal sections show TH-immunoreactive dopaminergic neurons in the SNpc of *LRRK* DKO and WT mice at the ages of 20 and 25 months. ***B***, Stereological neuron count reveals that the number of TH+ dopaminergic neurons in the SNpc of *LRRK* DKO mice at 20 months (10,356.0 ± 852.1) is markedly reduced, compared with WT mice (14,514.0 ± 549.4; $F_{(1,19)} = 13.29$, $p = 0.0017$; $p = 0.0005$, two-way ANOVA with Bonferroni's *post hoc* multiple comparisons). By 25 months of age, the reduction of dopaminergic neurons in the SNpc of *LRRK* DKO mice (8342.9 ± 306.7) is even more severe, compared with WT mice (12,013.3 ± 742.9, $p = 0.0005$). ***C***, Nissl staining of coronal sections of *LRRK* DKO and WT brains at 25 months of age shows normal gross brain morphology in *LRRK* DKO mice. ***D***, Quantification indicates that the volume of the neocortex in *LRRK* DKO mice (36.79 ± 0.69 mm^3) and WT controls (35.57 ± 1.32 mm^3) is similar ($p = 0.4090$, unpaired two-tailed Student's *t* test). ***E***, NeuN staining of coronal sections of *LRRK* DKO brains and WT controls at 25 months of age. ***F***, Stereological quantification of the number of NeuN+ neurons in the neocortex shows similar numbers of cortical neurons in *LRRK* DKO (4.93 ± 0.10 × 106) and WT brains (5.09 ± 0.31 × 106, $p = 0.6073$, unpaired two-tailed Student's *t* test) at 25 months of age. The value in the column indicates the number of the mice used in each experiment. All data are expressed as mean ± SEM. Red filled and open circles represent data obtained from individual male and female mice, respectively, and no sex-specific difference was found within the genotypic group ($p > 0.05$; specific *p* values can be found in Extended Data Figure 4-1); ***$p < 0.001$. Scale bar, 100 μm.

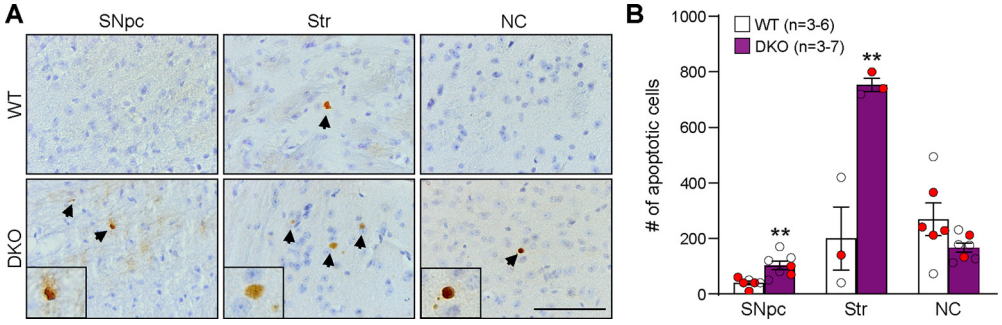

Figure 5. Increases of apoptosis in the SNpc and striatum of *LRRK* DKO mice at 25 months of age. **A**, Representative images of active Caspase-3 immunostaining show active Caspase-3-immunoreactive apoptotic cells (black arrowheads). ***B***, Quantification of active Caspase-3+ cells reveals significant increases of apoptotic cells in the SNpc (WT, 40.0 ± 6.8; DKO, 102.9 ± 15.4; $p = 0.0048$, unpaired two-tailed Student's *t* test) and the striatum (WT, 200.0 ± 113.7; DKO, 753.3 ± 24.0, $p = 0.0089$) of *LRRK* DKO mice, relative to WT mice, whereas the number of apoptotic cells is not significantly different in the neocortex (NC) between *LRRK* DKO mice (167.1 ± 17.0) and WT controls (269.2 ± 59.0, $p = 0.1023$). The value in the column indicates the number of the mice used in each experiment. All data are expressed as mean ± SEM. Red filled and open circles represent data obtained from individual male and female mice, respectively, and no sex-specific difference was found within the genotypic group ($p > 0.05$; specific *p* values can be found in Extended Data Figure 5-1); *$p < 0.05$, **$p < 0.01$. Scale bar, 100 μm.

Bonferroni's *post hoc* multiple comparisons; Fig. 1*D*). These results show that *LRRK* DKO mice exhibit impaired motor coordination before the onset of dopaminergic neuron loss, and the motor deficits worsen in aged DKO mice.

Age-dependent reduction of evoked DA release in *LRRK* DKO mice

We further examined whether dopaminergic neurotransmission is affected in *LRRK* DKO mice. We used fast-scan cyclic voltammetry to measure evoked DA release in the dorsal striatum of *LRRK* DKO and wild-type mice at the ages of 2, 8–10, and 15–16 months (Fig. 2). We found that there was no significant difference in peak DA concentration on five pulses of stimulation between *LRRK* DKO and wild-type mice at the ages of 2 months ($p = 0.8225$, unpaired two-tailed Student's *t* test) and 8–10 months ($p = 0.3314$; Fig. 2*D*). However, *LRRK* DKO mice at 15–16 months of age showed a significant reduction of DA concentration (1.16 ± 0.11 μM), compared with wild-type controls (1.16 ± 0.11 μM; $p = 0.0385$; Fig. 2*D*). There was no difference in the paired-pulse ratio between *LRRK* DKO and wild-type mice for the ages of 2 months ($p = 0.8898$, unpaired two-tailed Student's *t* test), 8-10 months ($p = 0.7619$) and 15–16 months ($p = 0.7560$; Fig. 2*E*). These results indicate that inactivation of LRRK results in age-dependent reduction of evoked DA release in the striatum.

Age-dependent loss of TH+ dopaminergic terminals in the striatum of *LRRK* DKO mice

To determine whether *LRRK* DKO mice exhibit dopaminergic terminal degeneration, we performed immunohistochemical analysis of *LRRK* DKO and wild-type mice at the ages of 2–25 months using an antibody specific for TH to label dopaminergic terminals in the striatum (Fig. 3*A*). Quantitative analysis revealed an age-dependent reduction of TH immunoreactivity in the striatum of *LRRK* DKO mice compared with wild-type controls, suggesting an age-dependent loss of TH+ dopaminergic terminals in the striatum (Fig. 3*B*). The reduction of TH+ dopaminergic terminals in the striatum becomes more pronounced as *LRRK* DKO mice age with ~21% reduction at the ages of 15 months ($p = 0.0378$) and 20 months ($p = 0.0088$) and ~30% reduction at 25 months ($p < 0.0001$; Fig. 3B).

Selective loss of dopaminergic neurons in the SNpc of *LRRK* DKO mice

We performed immunohistochemical analysis of *LRRK* DKO mice and wild-type controls at the ages of 20 and 25 months and quantified the number of TH+ dopaminergic neurons in the SNpc (Fig. 4*A*). Stereological quantification showed that the number of TH+ dopaminergic neurons in the SNpc of *LRRK* DKO mice is significantly reduced (~28%) at 20 months (10,356.0 ± 852.1), relative to wild-type controls (14,514.0 ± 549.4; $F_{(1,19)} = 13.29$, $p = 0.0017$, $p = 0.0005$, two-way ANOVA with Bonferroni's *post hoc* comparison; Fig. 4*B*). By 25 months of age, the reduction (~31%) of dopaminergic neurons in the SNpc of *LRRK* DKO mice (8342.9 ± 306.7) is even more severe, compared with wild-type mice (12,013.3 ± 742.9; $p = 0.0005$, Fig. 4*B*).

Interestingly, the cerebral cortex is unaffected in *LRRK* DKO mice at 25 months of age (Fig. 4*C–F*). The volume of the neocortex quantified using serial coronal sections is unchanged in *LRRK* DKO mice (36.79 ± 0.69 mm^3), compared with wild-type controls (35.57 ± 1.32 mm^3, $p = 0.4090$, unpaired two-tailed Student's *t* test; Fig. 4*D*). The number of neurons assessed by stereological quantification of NeuN+ cells in the neocortex is also similar between *LRRK* DKO (4.93 ± 0.10 × 106) and wild-type mice (5.09 ± 0.31 × 106, $p = 0.6073$; Fig. 4*F*). These results show that age-dependent neurodegeneration caused by loss of LRRK is selective and does not affect the cerebral cortex.

We also evaluated apoptosis in *LRRK* DKO mice and wild-type controls at 25 months of age using an antibody specific for active Caspase-3 to label apoptotic cells (Fig. 5*A*). We found that there are more active Caspase-3+ apoptotic cells in the SNpc of *LRRK* DKO mice relative to wild-type mice ($p = 0.0048$, unpaired two-tailed Student's *t* test; Fig. 5*B*). In the striatum, there are also significantly more apoptotic cells in *LRRK* DKO mice than in wild-type mice ($p = 0.0089$; Fig. 5*B*). However, the number of apoptotic cells in the neocortex is similar between wild-type and *LRRK* DKO mice ($p = 0.1023$; Fig. 5*B*).

Accumulation of autophagic vacuoles in surviving SNpc neurons lacking LRRK

We further performed quantitative EM analysis of *LRRK* DKO mice at 25 months to evaluate ultrastructural changes in surviving neurons of the SNpc (Fig. 6). We found that there are more electron-dense vacuoles in SNpc neurons of *LRRK* DKO mice, compared with wild-type controls (Fig. 6*A*,*C*). Higher power

views further revealed the presence of large autophagic and autolysosomal vacuoles as well as lipofuscin granules in neuronal profiles of *LRRK* DKO mice (Fig. 6*D–G*). Quantitative analysis showed that the average number of vacuoles in the SNpc of *LRRK* DKO mice (9.8 ± 1.0) is significantly increased, compared with wild-type mice (4.0 ± 0.4, $p < 0.0001$, unpaired two-tailed Student's *t* test; Fig. 6*H*). Furthermore, the percentage of *LRRK* DKO neuronal profiles (60.1 ± 14.1%) containing large numbers of electron-dense vacuoles (>7 per neuronal profile) is greatly elevated, compared with that from wild-type mice (14.1 ± 7.3%, $p = 0.0276$, unpaired two-tailed Student's *t* test).

Elevated microgliosis in the SNpc of *LRRK* DKO mice

Because microgliosis often accompanies ongoing neurodegeneration (Lobsiger and Cleveland, 2007; Tabuchi et al., 2009; Heneka et al., 2010; Watanabe et al., 2014; Kang and Shen, 2020), we further evaluated microgliosis in the SNpc of *LRRK* DKO and wild-type mice. We performed immunohistochemical analysis of Iba1, which labels microglia, and TH, which marks dopaminergic neurons and processes, thus showing the boundary of the SNpc (Fig. 7*A*). Quantification of Iba1+ cells in the SNpc showed a significant increase of Iba1+ cells in *LRRK* DKO mice (5097 ± 127), compared with wild-type controls (3187 ± 72, $p < 0.0001$, unpaired two-tailed Student's *t* test, Fig. 7*B*). However, there is no significant difference in the number of Iba1 + 1 microglia in the neocortex of *LRRK* DKO mice (8.7 ± 0.3 × 105) and wild-type controls (8.1 ± 0.3 × 105, $p = 0.1263$, unpaired two-tailed Student's *t* test; Fig. 7*C*, *D*). Thus, elevated microgliosis is associated with loss of dopaminergic neurons in the SNpc of *LRRK* DKO mice.

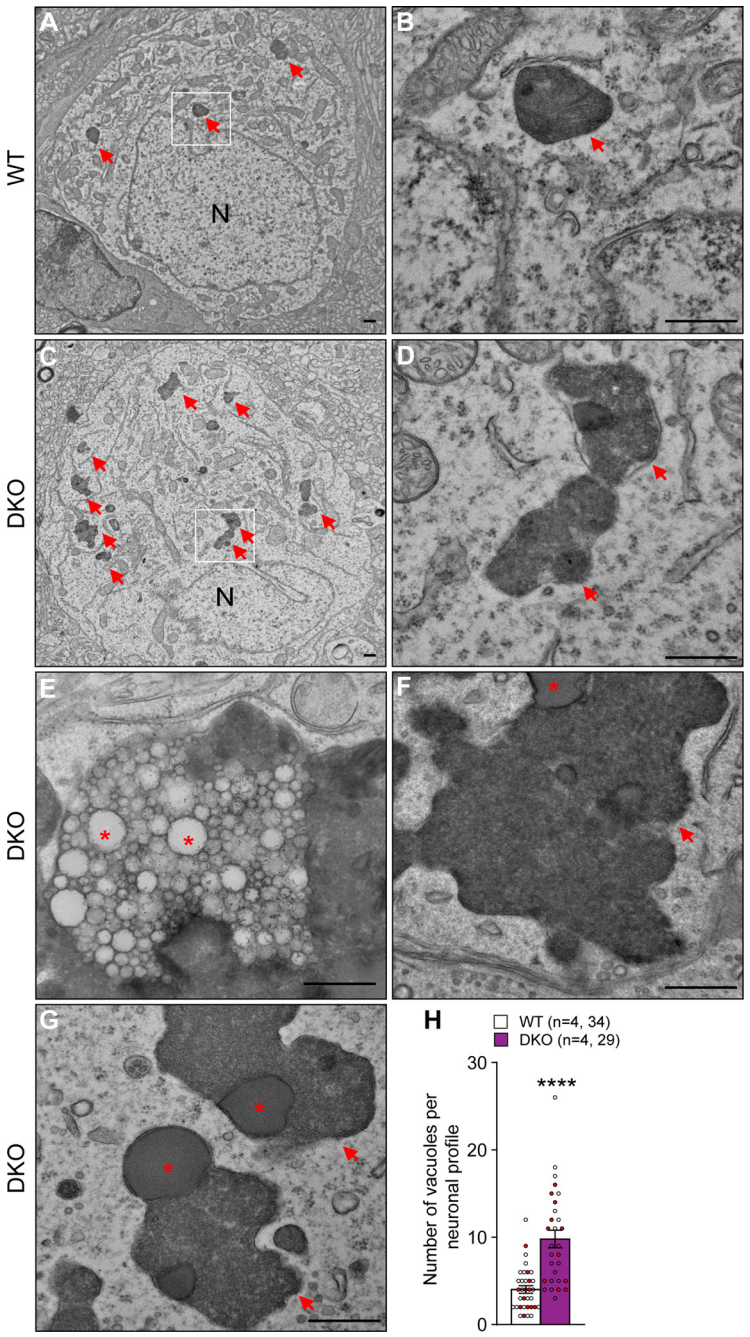

Figure 6. Accumulation of large autophagy vacuoles in the SNpc of *LRRK* DKO mice at 25 months of age. ***A–D***, Representative EM images showing electron-dense vacuoles (arrowheads) in the SNpc neurons of WT and *LRRK* DKO mice (***A***, ***C***). Higher power views of the boxed areas in ***A*** and ***C*** showing large autolysosome (arrowheads) vacuoles (***B***, ***D***). ***E–G***, Higher power views showing large vacuoles including lipofuscin inclusions (asterisks). ***H***, The average number of electron-dense vacuoles (>0.5 μm in diameter) in the SNpc of *LRRK* DKO mice (9.8 ± 1.0) is significantly increased compared with WT controls (4.0 ± 0.4, $p < 0.0001$, unpaired two-tailed Student's *t* test). The value in parentheses indicates the number of mice (left) and neuron profiles (right) used in each experiment. All data are expressed as mean ± SEM. Red filled and open circles represent data obtained from individual male and female mice, respectively, and no sex-specific difference was found within the WT or DKO group ($p > 0.05$; specific *p* values can be found in Extended Data Figure 6-1); *$p < 0.05$, ****$p < 0.0001$. Scale bar, 0.5 μm.

Discussion

LRRK2 mutations are the most common genetic cause of sporadic and familial PD, highlighting the importance of LRRK2 in PD pathogenesis. Although inactivation of LRRK2 does not cause DA neurodegeneration (Tong et al., 2010), loss of LRRK2 and its functional homolog LRRK1 results in loss of dopaminergic neurons in the SNpc at the age of 14–15 months (Giaime et al., 2017). In the current study, we performed behavioral, neurochemical, histological, and EM analyses of *LRRK* DKO female and male mice up to 25 months of age. Interestingly, we found that *LRRK* DKO mice exhibit motor deficits at 12 months of age before the onset of dopaminergic neuron loss (Fig. 1). We further observed age-dependent loss of DA axonal terminals and decreases of evoked DA release in the striatum of *LRRK* DKO mice (Figs. 2, 3). By 20–25 months of age, *LRRK* DKO mice exhibit a 28–31% reduction of dopaminergic neurons in the SNpc, which is associated with enhanced apoptotic cell

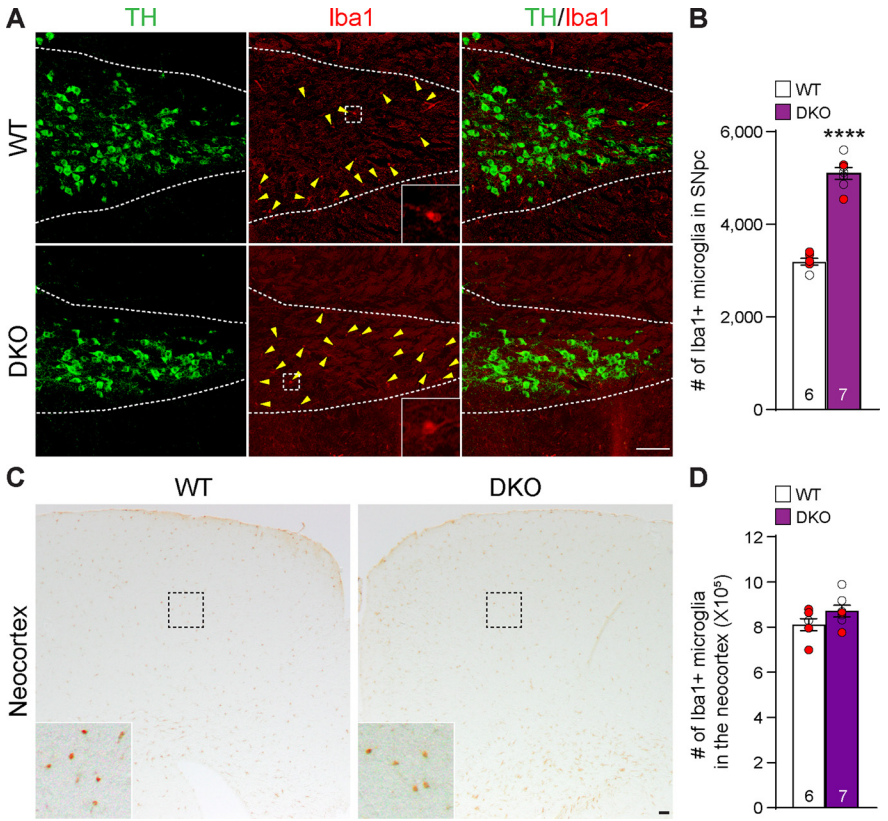

Figure 7. Elevated microgliosis in the SNpc of *LRRK* DKO mice. ***A***, Representative images of Iba1+ microglia (red, marked by yellow arrowheads) and TH immunoreactivity (green) in the SNpc of *LRRK* DKO mice and WT controls at 25 months of age. ***B***, Quantification of Iba1+ microglia shows a significant increase in the number of Iba1+ microglia in the SNpc of *LRRK* DKO mice (5097.1 ± 127.0), compared with WT mice (3186.7 ± 72.0; $p < 0.0001$, unpaired two-tailed Student's *t* test). ***C***, Representative images of Iba1+ microglia in the neocortex of *LRRK* DKO mice and WT controls at 25 months of age. ***D***, Stereological quantification shows that the number of Iba1+ cells in the neocortex of *LRRK* DKO mice (8.7 ± 0.3 × 105) and WT controls (8.1 ± 0.3 × 105) is similar ($p = 0.1263$, unpaired two-tailed Student's *t* test). The value in the column indicates the number of mice used in each experiment. Red filled and open circles represent data obtained from individual male and female mice, respectively. No sex-specific difference in microgliosis was found within the WT or DKO group ($p > 0.05$; specific *p* values can be found in Extended Data Figure 7-1). All data are expressed as mean ± SEM; ****$p < 0.0001$. Scale bar, 100 μm.

death and elevated microgliosis (Figs. 4, 5, 7). Furthermore, surviving SNpc neurons in *LRRK* DKO mice accumulate a large number of autophagic and autolysosomal vacuoles (Fig. 6). However, the cerebral cortex of *LRRK* DKO mice at 25 months of age is still unaffected, as shown by a normal cortical volume and neuron number as well as an unchanged number of apoptotic cells and microglia (Figs. 4, 5, 7). Thus, our findings demonstrate that *LRRK* DKO mice recapitulate several key features of PD, such as motor deficits, progressive dopaminergic axonal degeneration in the striatum, impairment of DA neurotransmission, and substantial loss of dopaminergic neurons in the SNpc.

Manipulation of genes linked to familial PD has largely failed to produce mouse models that recapitulate the cardinal feature of PD, namely age-dependent, selective, progressive dopaminergic neuron loss in the SNpc, which has hampered therapeutic development and identification of molecular pathways underlying dopaminergic neurodegeneration. For example, mutant mice lacking Parkin, DJ-1, or PINK1 alone or all of them do not develop dopaminergic neurodegeneration during the mouse life span (Goldberg et al., 2003; Itier et al., 2003; Goldberg et al., 2005; Kim et al., 2005; Kitada et al., 2007; Yamaguchi and Shen, 2007; Kitada et al., 2009). *LRRK2* transgenic and knock-in mice have largely failed to develop substantial loss of dopaminergic neurons (Lin et al., 2009; Tong et al., 2009; Tsika et al., 2014; Yue et al., 2015). In contrast to these PD mutant mice, *LRRK* DKO mice develop selective, age-dependent, robust dopaminergic neurodegeneration, including progressive loss of dopaminergic terminals in the striatum and progressive loss of dopaminergic neurons in the SNpc, resembling the neuropathology of PD patients carrying LRRK2 mutations (Paisán-Ruíz et al., 2004; Zimprich et al., 2004). Similar to *Parkin*$^{-/-}$ and *PINK1*$^{-/-}$ mice (Goldberg et al., 2005; Kitada et al., 2007), evoked DA release is also reduced in the striatum of *LRRK* DKO mice. The reduction of TH+ dopaminergic neurons in the SNpc of *LRRK* DKO mice is not because of the loss of TH expression, as NeuN+ cells are also decreased in the SNpc of *LRRK* DKO mice (Giaime et al., 2017). Furthermore, we also observed motor deficits in *LRRK* DKO mice at 12–24 months of age. The fact that there are marked increases of apoptotic cells in the striatum of *LRRK* DKO mice raises the possibility that loss of medium spiny neurons in the striatum may contribute to motor deficits in *LRRK* DKO mice.

Our earlier studies of *LRRK2* KO mice revealed striking autophagy impairments in the kidney, indicating that LRRK2 is a key regulator of the autophagy-lysosomal pathway (Tong et al., 2010; 2012; Tong and Shen, 2012). EM analysis of *LRRK* DKO mice at the ages of 3, 10, 15, and 25 months showed striking accumulation of autophagic and autolysosomal vacuoles in the SNpc. Interestingly, wild-type mice also accumulate electron-dense vacuoles in the SNpc in an age-dependent manner; by 25 months of age ~14% of neurons in the SNpc of wild-type mice accumulate large numbers (at least eight) of vacuoles. However, ~60% of surviving neurons in the SNpc of *LRRK* DKO mice at 25 months of age contain at least eight vacuoles, and some of the lipofuscin inclusions are very large (>3 μm). These findings further support a key regulatory role of LRRK in autophagic and lysosomal function and suggest that autophagic impairment may contribute to the early dopaminergic neuron death in *LRRK* DKO mice. The molecular mechanism by which LRRK regulates the autophagy-lysosomal pathway is still unclear and awaits further investigation, and *LRRK* DKO mice are invaluable for further identification of molecular mechanisms underlying LRRK2 function and dysfunction.

In summary, our genetic studies demonstrate that germline inactivation of LRRK1/2 results in selective, substantial dopaminergic neurodegeneration, as evidenced by age-dependent loss of dopaminergic terminals in the striatum and dopaminergic neurons in the SNpc, whereas the cerebral cortex is spared, highlighting a crucial requirement of LRRK in the survival of dopaminergic neurons during aging. Future studies using dopaminergic neuron-specific *LRRK1/2* conditional double knock-

out mice will determine whether LRRK plays a cell autonomous and/or noncell autonomous role in dopaminergic neuron survival in the aging brain. Furthermore, our findings raise the possibility that LRRK2 mutations may lead to dopaminergic neurodegeneration and PD via a partial loss-of-function mechanism. Further investigations will be needed to distinguish between a toxic gain-of-function and a partial loss-of-function pathogenic mechanism, as this will have a profound impact on LRRK2-based therapeutic development; a toxic gain-of-function mechanism would require inhibition of LRRK2 function or kinase activity as PD therapy, whereas a partial loss-of-function pathogenic mechanism would point to enhancement of LRRK2 function as a treatment of PD.

References

Bosgraaf L, Van Haastert PJ (2003) Roc, a Ras/GTPase domain in complex proteins. Biochim Biophys Acta 1643:5–10.

Cookson MR (2016) Cellular functions of LRRK2 implicate vesicular trafficking pathways in Parkinson's disease. Biochem Soc Trans 44:1603–1610.

Di Fonzo A, Rohé CF, Ferreira J, Chien HF, Vacca L, Stocchi F, Guedes L, Fabrizio E, Manfredi M, Vanacore N, Goldwurm S, Breedveld G, Sampaio C, Meco G, Barbosa E, Oostra BA, Bonifati V (2005) A frequent LRRK2 gene mutation associated with autosomal dominant Parkinson's disease. Lancet 365:412–415.

Erb M, Moore DJ (2020) LRRK2 and the endolysosomal system in Parkinson's disease. J Parkinsons Dis 10:1271–1291.

Giaime E, Tong Y, Wagner LK, Yuan Y, Huang G, Shen J (2017) Age-dependent dopaminergic neurodegeneration and impairment of the autophagy-lysosomal pathway in LRRK-deficient mice. Neuron 96:796–807.e6.

Gilks WP, Abou-Sleiman PM, Gandhi S, Jain S, Singleton A, Lees AJ, Shaw K, Bhatia KP, Bonifati V, Quinn NP, Lynch J, Healy DG, Holton JL, Revesz T, Wood NW (2005) A common LRRK2 mutation in idiopathic Parkinson's disease. Lancet 365:415–416.

Goldberg MS, Fleming SM, Palacino JJ, Cepeda C, Lam HA, Bhatnagar A, Meloni EG, Wu N, Ackerson LC, Klapstein GJ, Gajendiran M, Roth BL, Chesselet MF, Maidment NT, Levine MS, Shen J (2003) Parkin-deficient mice exhibit nigrostriatal deficits but not loss of dopaminergic neurons. J Biol Chem 278:43628–43635.

Goldberg MS, Pisani A, Haburcak M, Vortherms TA, Kitada T, Costa C, Tong Y, Martella G, Tscherter A, Martins A, Bernardi G, Roth BL, Pothos EN, Calabresi P, Shen J (2005) Nigrostriatal dopaminergic deficits and hypokinesia caused by inactivation of the familial Parkinsonism-linked gene DJ-1. Neuron 45:489–496.

Hatano T, Funayama M, Kubo SI, Mata IF, Oji Y, Mori A, Zabetian CP, Waldherr SM, Yoshino H, Oyama G, Shimo Y, Fujimoto KI, Oshima H, Kunii Y, Yabe H, Mizuno Y, Hattori N (2014) Identification of a Japanese family with LRRK2 p.R1441G-related Parkinson's disease. Neurobiol Aging 35:2656.e2617–2656.e2623.

Heneka MT, Rodríguez JJ, Verkhratsky A (2010) Neuroglia in neurodegeneration. Brain Res Rev 63:189–211.

Hernandez DG, Paisan-Ruíz C, McInerney-Leo A, Jain S, Meyer-Lindenberg A, Evans EW, Berman KF, Johnson J, Auburger G, Schäffer AA, Lopez GJ, Nussbaum RL, Singleton AB (2005) Clinical and positron emission tomography of Parkinson's disease caused by LRRK2. Ann Neurol 57:453–456.

Itier JM, et al. (2003) Parkin gene inactivation alters behaviour and dopamine neurotransmission in the mouse. Hum Mol Genet 12:2277–2291.

Kachergus J, Mata IF, Hulihan M, Taylor JP, Lincoln S, Aasly J, Gibson JM, Ross OA, Lynch T, Wiley J, Payami H, Nutt J, Maraganore DM, Czyzewski K, Styczynska M, Wszolek ZK, Farrer MJ, Toft M (2005) Identification of a novel LRRK2 mutation linked to autosomal dominant parkinsonism: evidence of a common founder across European populations. Am J Hum Genet 76:672–680.

Kang J, Shen J (2020) Cell-autonomous role of Presenilin in age-dependent survival of cortical interneurons. Mol Neurodegener 15:72.

Kang J, Watanabe H, Shen J (2021) Protocols for assessing neurodegenerative phenotypes in Alzheimer's mouse models. STAR Protoc 2:100654.

Kim SY, Kim MS, Chun MM (2005) Concurrent working memory load can reduce distraction. Proc Natl Acad Sci U S A 102:16524–16529.

Kitada T, Pisani A, Porter DR, Yamaguchi H, Tscherter A, Martella G, Bonsi P, Zhang C, Pothos EN, Shen J (2007) Impaired dopamine release and synaptic plasticity in the striatum of PINK1-deficient mice. Proc Natl Acad Sci U S A 104:11441–11446.

Kitada T, Pisani A, Karouani M, Haburcak M, Martella G, Tscherter A, Platania P, Wu B, Pothos EN, Shen J (2009) Impaired dopamine release and synaptic plasticity in the striatum of parkin−/− mice. J Neurochem 110:613–621.

Kluss JH, Mamais A, Cookson MR (2019) LRRK2 links genetic and sporadic Parkinson's disease. Biochem Soc Trans 47:651–661.

Lesage S, et al. (2007) LRRK2 exon 41 mutations in sporadic Parkinson disease in Europeans. Arch Neurol 64:425–430.

Lin X, Parisiadou L, Gu XL, Wang L, Shim H, Sun L, Xie C, Long CX, Yang WJ, Ding J, Chen ZZ, Gallant PE, Tao-Cheng JH, Rudow G, Troncoso JC, Liu Z, Li Z, Cai H (2009) Leucine-rich repeat kinase 2 regulates the progression of neuropathology induced by Parkinson's-disease-related mutant alpha-synuclein. Neuron 64:807–827.

Lobsiger CS, Cleveland DW (2007) Glial cells as intrinsic components of non-cell-autonomous neurodegenerative disease. Nat Neurosci 10:1355–1360.

Mata IF, Taylor JP, Kachergus J, Hulihan M, Huerta C, Lahoz C, Blazquez M, Guisasola LM, Salvador C, Ribacoba R, Martinez C, Farrer M, Alvarez V (2005a) LRRK2 R1441G in Spanish patients with Parkinson's disease. Neurosci Lett 382:309–311.

Mata IF, Kachergus JM, Taylor JP, Lincoln S, Aasly J, Lynch T, Hulihan MM, Cobb SA, Wu RM, Lu CS, Lahoz C, Wszolek ZK, Farrer MJ (2005b) LRRK2 pathogenic substitutions in Parkinson's disease. Neurogenetics 6:171–177.

Matsuura K, Kabuto H, Makino H, Ogawa N (1997) Pole test is a useful method for evaluating the mouse movement disorder caused by striatal dopamine depletion. J Neurosci Methods 73:45–48.

Nichols WC, Pankratz N, Hernandez D, Paisán-Ruíz C, Jain S, Halter CA, Michaels VE, Reed T, Rudolph A, Shults CW, Singleton A, Foroud T. (2005) Genetic screening for a single common LRRK2 mutation in familial Parkinson's disease. Lancet 365:410–412.

Paisán-Ruíz C, et al. (2004) Cloning of the gene containing mutations that cause PARK8-linked Parkinson's disease. Neuron 44:595–600.

Roosen DA, Cookson MR (2016) LRRK2 at the interface of autophagosomes, endosomes and lysosomes. Mol Neurodegener 7:73.

Ruifrok AC, Johnston DA (2001) Quantification of histochemical staining by color deconvolution. Anal Quant Cytol Histol 23:291–299.

Schindelin J, Arganda-Carreras I, Frise E, Kaynig V, Longair M, Pietzsch T, Preibisch S, Rueden C, Saalfeld S, Schmid B, Tinevez JY, White DJ, Hartenstein V, Eliceiri K, Tomancak P, Cardona A (2012) Fiji: an open-source platform for biological-image analysis. Nat Methods 9:676–682.

Shen J (2004) Protein kinases linked to the pathogenesis of Parkinson's disease. Neuron 44:575–577.

Shu L, Zhang Y, Sun Q, Pan H, Tang B (2019) A comprehensive analysis of population differences in LRRK2 variant distribution in Parkinson's disease. Front Aging Neurosci 11:13.

Tabuchi K, Chen G, Südhof TC, Shen J (2009) Conditional forebrain inactivation of nicastrin causes progressive memory impairment and age-related neurodegeneration. J Neurosci 29:7290–7301.

Takanashi M, Funayama M, Matsuura E, Yoshino H, Li Y, Tsuyama S, Takashima H, Nishioka K, Hattori N (2018) Isolated nigral degeneration without pathological protein aggregation in autopsied brains with LRRK2 p.R1441H homozygous and heterozygous mutations. Acta Neuropathol Commun 6:105.

Tong Y, Shen J (2012) Genetic analysis of Parkinson's disease-linked leucine-rich repeat kinase 2. Biochem Soc Trans 40:1042–1046.

Tong Y, Pisani A, Martella G, Karouani M, Yamaguchi H, Pothos EN, Shen J (2009) R1441C mutation in LRRK2 impairs dopaminergic neurotransmission in mice. Proc Natl Acad Sci U S A 106:14622–14627.

Tong Y, Yamaguchi H, Giaime E, Boyle S, Kopan R, Kelleher RJ 3rd, Shen J (2010) Loss of leucine-rich repeat kinase 2 causes impairment of protein degradation pathways, accumulation of alpha-synuclein, and apoptotic cell death in aged mice. Proc Natl Acad Sci U S A 107:9879–9884.

Tong Y, Giaime E, Yamaguchi H, Ichimura T, Liu Y, Si H, Cai H, Bonventre JV, Shen J (2012) Loss of leucine-rich repeat kinase 2 causes age-dependent bi-phasic alterations of the autophagy pathway. Mol Neurodegener 7:2–2.

Tsika E, Kannan M, Foo CS, Dikeman D, Glauser L, Gellhaar S, Galter D, Knott GW, Dawson TM, Dawson VL, Moore DJ (2014) Conditional expression of Parkinson's disease-related R1441C LRRK2 in midbrain dopaminergic neurons of mice causes nuclear abnormalities without neurodegeneration. Neurobiol Dis 71:345–358.

Vidyadhara DJ, Lee JE, Chandra SS (2019) Role of the endolysosomal system in Parkinson's disease. J Neurochem 150:487–506.

Watanabe H, Iqbal M, Zheng J, Wines-Samuelson M, Shen J (2014) Partial loss of presenilin impairs age-dependent neuronal survival in the cerebral cortex. J Neurosci 34:15912–15922.

Yamaguchi H, Shen J (2007) Absence of dopaminergic neuronal degeneration and oxidative damage in aged DJ-1-deficient mice. Mol Neurodegener 2:10.

Yamaguchi H, Shen J (2013) Histological analysis of neurodegeneration in the mouse brain. Methods Mol Biol 1004:91–113.

Yue M, Hinkle KM, Davies P, Trushina E, Fiesel FC, Christenson TA, Schroeder AS, Zhang L, Bowles E, Behrouz B, Lincoln SJ, Beevers JE, Milnerwood AJ, Kurti A, McLean PJ, Fryer JD, Springer W, Dickson DW, Farrer MJ, Melrose HL (2015) Progressive dopaminergic alterations and mitochondrial abnormalities in LRRK2 G2019S knock-in mice. Neurobiol Dis 78:172–195.

Zabetian CP, Samii A, Mosley AD, Roberts JW, Leis BC, Yearout D, Raskind WH, Griffith A (2005) A clinic-based study of the LRRK2 gene in Parkinson disease yields new mutations. Neurology 65:741–744.

Zimprich A, et al. (2004) Mutations in LRRK2 cause autosomal-dominant parkinsonism with pleomorphic pathology. Neuron 44:601–607.